Supporting Information

Dual-Mode Frequency Multiplier in Graphene-Base Hot Electron Transistor

Bor-Wei Liang[1], Min-Fang Li[1], Hung-Yu Lin[1], Kai-Shin Li[2], Jyun-Hong Chen[2], Jia-Min Shieh[2], Chien-Ting Wu[2], Kristan Bryan Simbulan[3], Ching-Yuan Su[4], Chieh-Hsiung Kuan[1] and Yann-Wen Lan[4,5*]

[1]Graduate Institute of Electronics Engineering, National Taiwan University, Taipei 10617, Taiwan
[2]Taiwan Semiconductor Research Institute, National Applied Research Laboratories, Hsinchu 30078, Taiwan

[3]Department of Mathematics and Physics, University of Santo Tomas, Manila 1008, Philippines

[4]Graduate Institute of Energy Engineering, National Central University, No. 300, Jhongda Rd., Jhongli, Taoyuan, 320317, Taiwan

[5]Department of Physics, National Taiwan Normal University, Taipei 11677, Taiwan

[6]Advanced Materials and Green Energy Research Center, National Taiwan Normal University, Taipei 11677, Taiwan

*****Corresponding Author e-mail address: ywlanblue@gmail.com

KEYWORDS: Dual-mode, Frequency multiplier, quantum tunneling, graphene transistor, 2D materials, frequency doubler

1. Raman spectra for graphene / MoS$_2$ / h-BN stacking

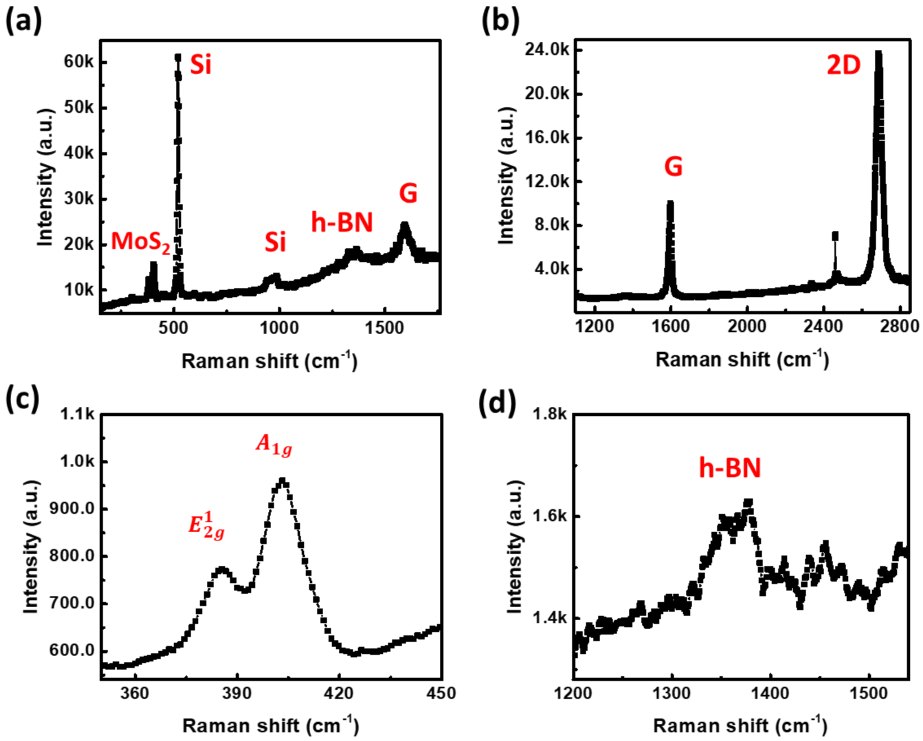

Figure S1. Raman spectra of the cross-section of our GHET for (a) all range spectrum, (b) graphene, (c) MoS$_2$, and (d) h-BN.

The Raman spectroscopic characterizations cross-section of the GHET and the peaks of the graphene, MoS$_2$, and hBN layers, which are used in these devices, are shown in **Figure S1**. **Figure S1a** reveals the MoS$_2$, Si, hBN, and graphene characteristic Raman peaks. **Figure S1b** presents the graphene Raman spectrum. The ratio between the G and 2D peaks (about 1:2) with a weak defect peak indicates a good quality monolayer graphene [1]. In **Figure S1c**, the peak separation of Raman peaks A_{1g} and E^1_{2g} is around 20.5 cm^{-1} indicating the presence of a monolayer CVD-MoS$_2$[2]. **Figure 2d** shows the characteristic Raman peak of hBN (1367cm^{-1}). [3]

2. Two-terminal transport characteristics for temperature-dependent measurement

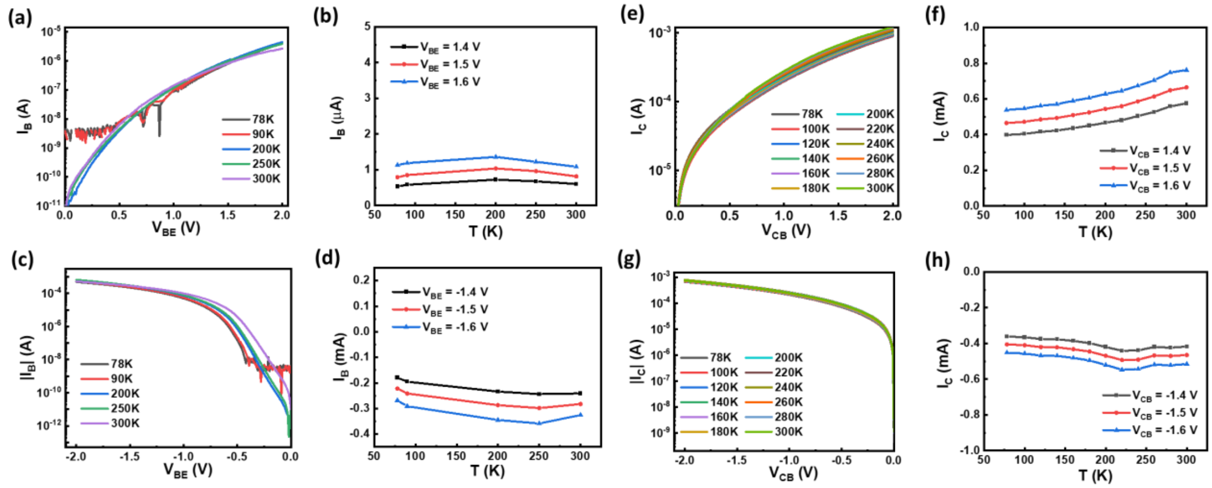

Figure S2. (a) The current-voltage (I_B – V_{BE}) characteristics of the device using a two-terminal measurement technique under different temperatures, where V_{BE} is larger than 0 V, **(b)** I_B - T at fixed bias V_{BE}. **(c)** I_B - V_{BE} under different temperatures, where $V_{BE} < 0$ V, **(d)** I_B - T at fixed bias V_{BE}. **(e)** The current-voltage (I_c – V_{CE}) characteristics via two-terminal measurement under different temperatures where V_{CE} is larger than 0 V, **(f)** I_C - T at fixed bias V_{CE}. **(g)** I_C – V_{CB} under different temperatures, where $V_{BE} < 0$ V, **(h)** I_C - T at fixed bias V_{CB}.

Figure S2 demonstrates the two-terminal measurement I-V curve from T = 300 K to T = 78 K. **Figure S2a** shows the I_B-V_{BE} curve at $V_{BE} > 0$ V, **Figure S2b** shows the corresponding I_B-T curve at certain fixed values of V_{BE}, while **Figure S2c** and **Figure S2d** show the same measurement method for $V_{BE} < 0$ V. These results demonstrate almost constant current levels at different temperatures at certain fixed V_{BE} and confirm the tunneling mechanism. Similar results are also shown in **Figure S2e-S2h** for the C-B terminal. Therefore, we have observed that the tunneling mechanism dominates the carrier transport at high applied bias in the B-E and C-B terminals.

3. Experimental and fitted I-V characteristics of device's emitter-base and collector-base terminals

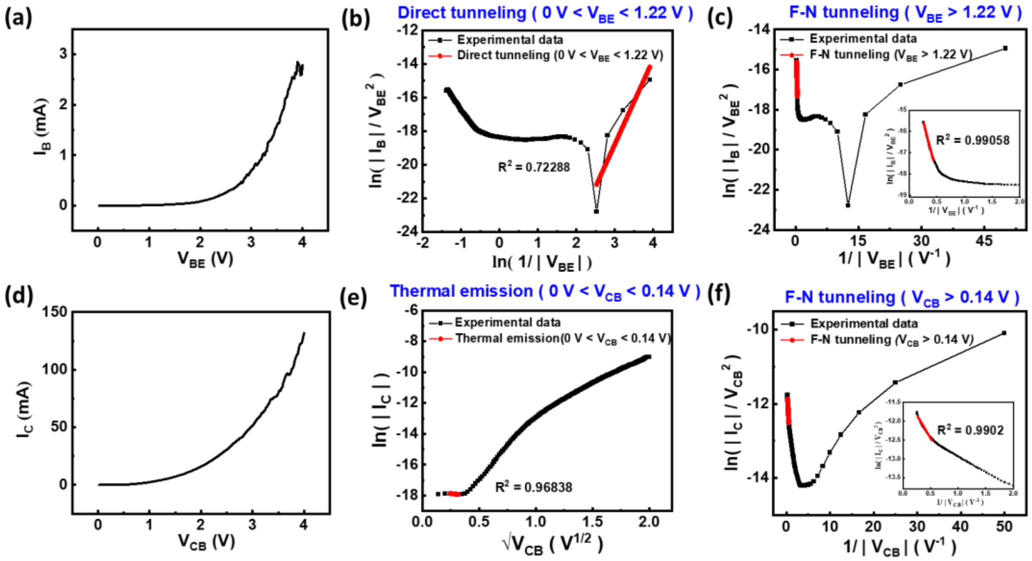

Figure S3. (a) I_B - V_{BE} for $V_{BE} > 0$ V. **(b)** Direct tunneling fitting of (a) for 0 V < V_{BE} < 1.22 V. **(c)** F-N tunneling fitting of (a) for $V_{BE} > 1.22$ V. **(d)** I_C - V_{CB} for $V_{CB} > 0$ V. **(e)** Thermionic emission fitting of (b) for 0 V < V_{CB} < 0.14 V. **(f)** F-N tunneling fitting of (b) for $V_{CB} > 0.14$ V.

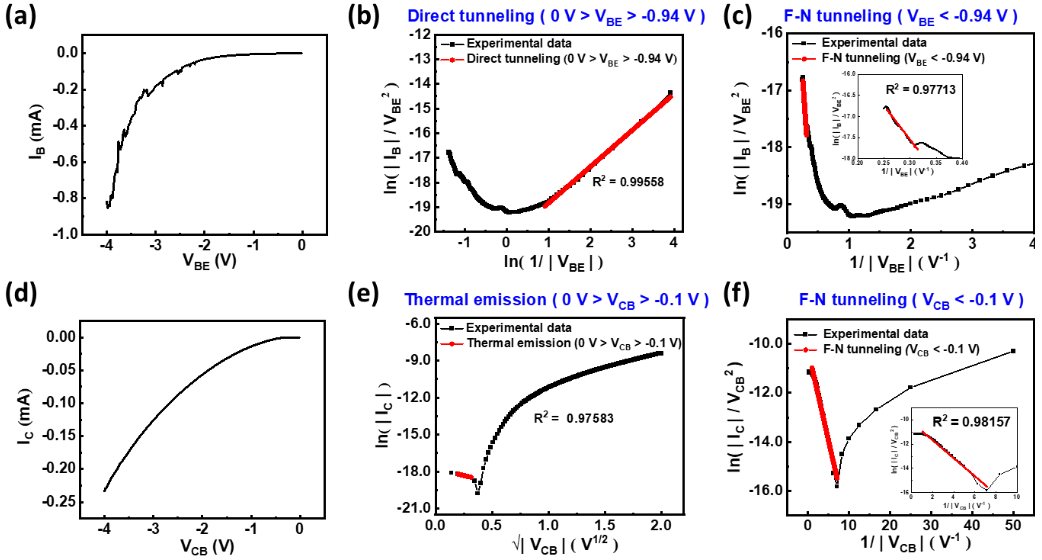

Figure S4. (a) I_B - V_{BE} for $V_{BE} < 0$ V. **(b)** Direct tunneling fitting of (a) for -0.94 V < V_{BE} < 0 V. **(c)** F-N tunneling fitting of (a) for $V_{BE} < -0.94$ V. **(d)** I_C - V_{CB} for $V_{CB} < 0$ V. **(e)** Thermionic emission fitting of (b) for -0.1 V < V_{CB} < 0 V. **(f)** F-N tunneling fitting of (b) for $V_{CB} < -0.1$ V.

Two-terminal current-voltage characteristics involving both the B-E and the B-C barriers at positive applied bias are shown in **Figure S3**. **Figure S3a** provides the current-voltage (I-V) characteristics measurement for the base current (i.e., emitter current) as a function of applied V_{BE}. The onset voltage V_{on} is about 1.22 V, and the current value is about a few micro-amperes. As implied in the band diagrams (**Figure 2** in the main text), quantum tunneling is the dominating carrier transport mechanism. Energy barriers for both SiO_2 (EB barrier) can be bent between the on-state and the off-state of the two terminals. Carrier transport through a barrier below the onset voltage can arise from several mechanisms such as Direct Tunneling or Thermal Emission) while Fowler−Nordheim (FN) tunneling is applied above the onset voltage. Figure S3b and **Figure S3c** show the fitting curve of the Direct tunneling (off-state) mechanism and FN tunneling (on-state). For the B-E terminal, the I-V relationship curve can be linearly fitted for the Direct tunneling mechanism (off-state) through the $\ln(I/V^2)$ versus $\ln(V^{-1})$ plot at $V_{BE} < 1.22$ V (**Figure S3b**).

The I-V relationship curve of the F-N tunneling (on-state) mechanism can also be analyzed on an ln(I) versus V^{-1} plot at $V_{BE} > 1.22$ V (**Figure S3c**).[4, 5] A good fit is achieved at higher V_{BE}, which confirms that the dominant transport mechanism is FN tunneling. Similar characteristics were revealed across the CB terminals, as shown in **Figure S3d -S3f**. The I-V relationship curve of the thermal emission (off-state) mechanism can be linearly fit on an ln(I) versus $\ln(V^{1/2})$ plot at $V_{CB} < 0.14$ V (**Figure S3e**). And the I-V relationship curve of the F-N tunneling (on-state) mechanism can also be studied on an ln(I) versus V^{-1} plot at $V_{CB} > 0.14$ V (**Figure S3f**). A similar result can also be performed in the negative applied base in GHET, as shown in **Figure S4**.

4. The DC measurement result of GHET

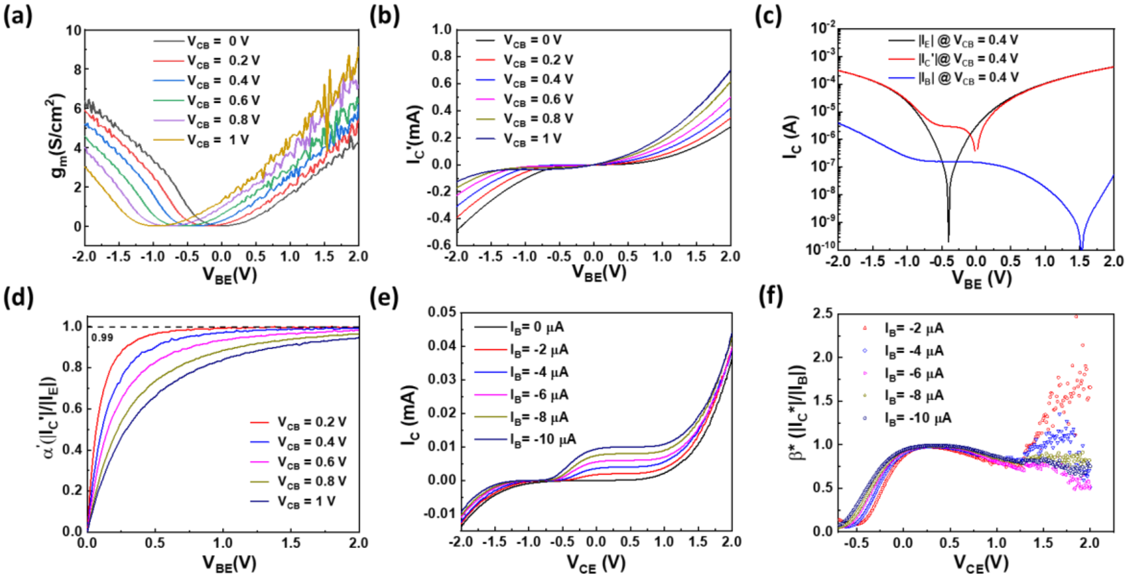

Figure S5 (a) The transconductance (g_m) and **(b)** I_C' with applied V_{CB}, via common-base measurement and **(c)** I-V_{CB} curves comparing the I_E, I_C' and I_B at V_{CB} = 0.4 V. **(d)** Common-base current gain (α*) as a function of V_{BE} at various V_{CB} levels Common-emitter characteristics for **(e)** I_C and **(f)** current gain (β*) tuned by V_{CE} at varying input base current (I_B).

The basic characteristic of GHET is shown in **Figure S5**. **Figure S5a** shows the transconductance (g_m), which is a noticeable increase at larger V_{BE}. This result indicates that the base-emitter and collector-base barriers are bent by applied V_{BE} so that the electron can tunnel through GHET devices. In order to extract the leakage current from the base to the collector, the corrected collector current (I_C') is defined as the difference between the original collector current (I_C ($V_{BE} \neq 0$)) and the collector current (I_C (V_{BE} = 0)) with no V_{BE} applied bias. **Figure S5b** shows the I_C'-V_{BE} characteristic curves with different values of V_{CB} applied. The electrical characteristic is similar to the I_C-V_{BE} (**Figure 2d**) within the on-state condition (Region I and Region III). **Figure S5c** shows the I-V_{CB} curves comparing the I_E, I_C' and I_B at V_{CB} = 0.4 V. The value of I_B is more than 2 orders smaller than the output current I_C', which indicates the small leakage current from base to collector.

One of the figures of merits for GHET is its common base current gain, $\alpha = |I_C|/|I_E|$. In our case, the common base current gain is defined as $\alpha' = |I_C'|/|I_E|$ to remove the concern of leakage current. **Figure S5d** shows that the α' gets closer to 0.992 and maintains a certain value at an applied bias greater than $V_{BE} = 1.25$ V, which is similar to the onset voltage of V_{BE} terminal (see **Figure S3c**).

The amplifier characteristics of the GHET under the common-emitter configuration can also be revealed. **Figure S5e** and **Figure S5f** show the I_C-V_{CE} curves and corresponding common base current gain (β^*) = $|I_C^*|/|I_B|$, respectively. Here, the I_C^* is also defined as the difference between the original collector current (I_C ($I_B \neq 0$)) and the collector current at zero input current (I_C ($I_B = 0$)) in order to extract the leakage current from the emitter to the collector. The maximum value of β^* is around 1.8 at $V_{CE} = 2$ V and $I_B = -2$ μA.

We also estimate the cut-off frequency by the RC time constant as the equation below.

$$f_T = \frac{g_m}{2\pi C}$$

where f_T is the cut-off frequency of GHET, g_m is the transconductance per area of GHET (about ~8 S/cm^2, see **Figure S5a**). *C* denotes the net capacitance per area of the 1.7 nm SiO_2 and 4 nm hBN in series. The capacitance is given by ε/d. d is the thickness of dielectric materials. The dielectric constant (ε) for hBN and SiO_2 is 3.29 and 3.9, respectively.[6, 7] The calculated f_T is about 5 MHz. This result shows that the device can only be applied to around MHz range in these specific devices.

5. The IV characteristic of GHET operated at $V_{BE} > 0$ and $V_{CB} < 0$

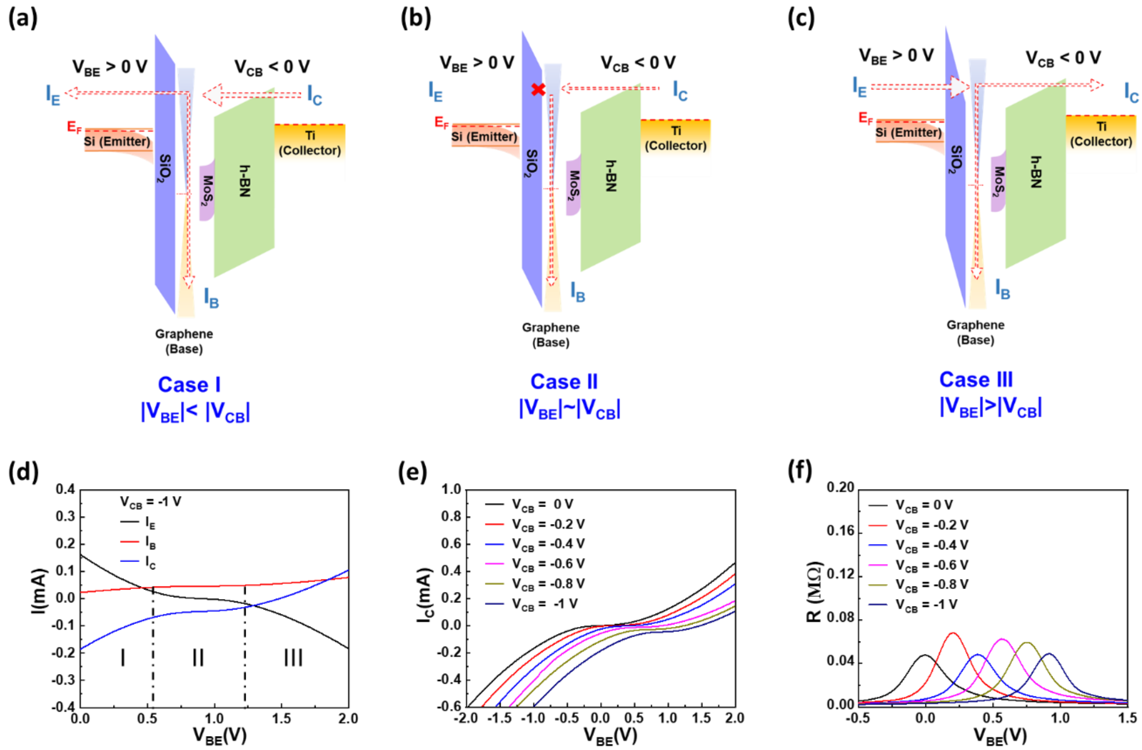

Figure S6 Energy band diagrams for $V_{BE} > 0$ and $V_{CB} < 0$. (a) Case I: $|V_{BE}| < |V_{CB}|$ (b) Case II: $|V_{BE}| \sim |V_{CB}|$ (c) Case III: $|V_{BE}| > |V_{CB}|$ (d) I-V_{BE} curves comparing the I_E, I_B, and I_C at fixed V_{CB} = -1 V under common-base operation. (e) I_C-V_{BE} curves at various values of negative V_{CB}. (f) R-V_{BE} curves controlled by various values of V_{CB}.

The electrical characteristics of GHET at negative V_{BC} applied are discussed in **Figure S6**. **Figure S6a-S6c** are the energy band diagrams at $V_{BE} > 0$ and $V_{CB} < 0$ for case I: $|V_{BE}| < |V_{CB}|$, case II: $|V_{BE}| \sim |V_{CB}|$, case III: $|V_{BE}| > |V_{CB}|$ conditions. The corresponding I-V_{BE} curves are demonstrated in **Figure S6d**. For case I ($|V_{BE}| < |V_{CB}|$), the hot carriers gain enough kinetic energy from the collector, passing through the collector-base barrier (hBN) and finally entering the base region. The native SiO_2 with applied positive V_{BE} creates a higher barrier to block some cold electrons from the graphene base and then forms the positive I_B. On the other hand, electrons with enough kinetic energy can tunnel through the emitter-base barrier and generate current I_C. If we increase V_{BE} further (Case II: $|V_{BE}| \sim |V_{CB}|$), the emitter-base tunneling barrier can block most of the electrons from base to emitter. Therefore, the value of I_E is close to 0. As the V_{BE} gets larger (Case III: $|V_{BE}| > |V_{CB}|$), the directions of I_C and I_E electrons are opposite to case I. The hot electrons can pass through the GHET from the emitter to the collector. On the other hand, the cold electrons are blocked by the collector base barrier (MoS_2/hBN) forming positive current I_B. I_C-V_{BE} curves at various negative V_{CB} and the corresponding R-V_{BE} curves are shown in **Figure S6e** and **Figure S6f**, respectively. According to these two figures, it can be found that the R peaks happen at Case II($|V_{BE}| \sim |V_{CB}|$) bias condition. Therefore, when a higher negative value of V_{CB} is applied, the R peak position will shift to a higher V_{BE} region.

7. The reproducible behavior of $P_{out, 3f}$ / $P_{out, 2f}$ contour plot in another device

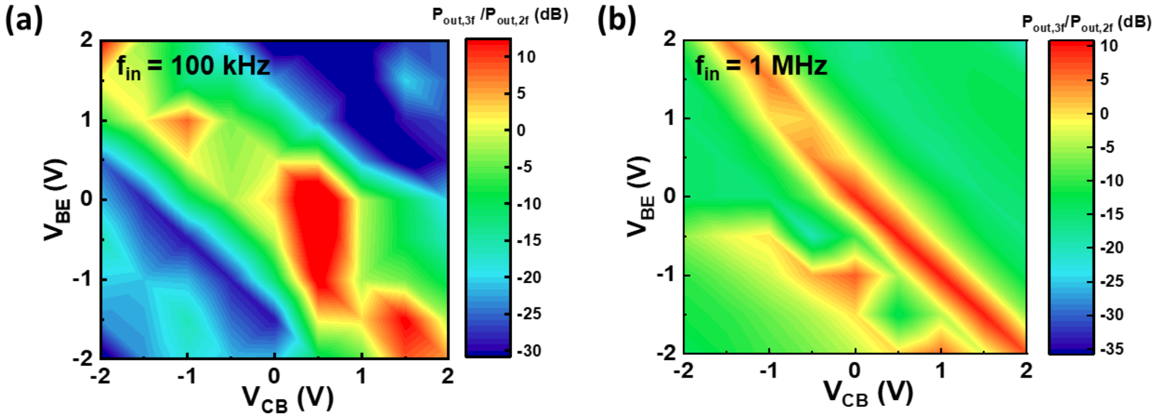

Figure S7. The contour plot of $P_{out, 3f}$ / $P_{out, 2f}$ under different values of applied bias given an (a) f_{in}= 100 kHz and (b) f_{in}= 1 MHz in another device.

We have fabricated many GHET devices with different collector areas. The results are repeatable and reproducible. The $P_{out, 3f}$ / $P_{out, 2f}$ contour plot of one of them is shown in **Figure S5,** in which the collector area is about 5×10^{-6} cm^2.

8. The limitation of operation frequency of the GHET

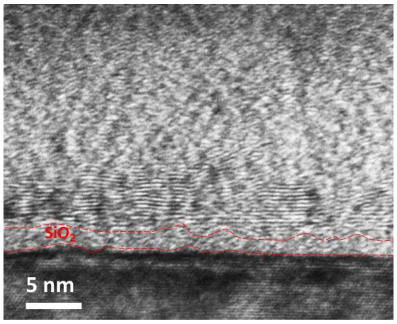

Figure S8. (a) TEM image showing the native SiO_2 thickness of the GHET. The thickness varies from 0.9 nm to 1.8 nm.

The operation frequency limitation is probably due to the native silicon dioxide thickness. We consider the FN tunneling model (shown below)[8] to estimate the transconductance (g_m) and the corresponding cut-off frequency of this kind of GHET design.

$$I(V) = \frac{A_{eff} m q^3 V^2}{8\pi h \phi_B d^2 m^*} \exp(\frac{-8\pi\sqrt{2m^*}\phi_B^{\frac{3}{2}} d}{3hqV})$$

where $q, m, m^*, h, d, A_{eff}, \phi_B,$ and V are elementary charge, electron mass, effective mass ($0.42\times m$ for SiO_2)[9], Plank's constant, SiO_2 thickness, effective area of devices (7.85×10^{-5} cm^2), barrier height (~2.96 eV) [10] and the applied bias. **Figure S8** shows the TEM image of the native SiO_2 thickness for the GHET. The SiO_2 thickness varies from 0.9 nm to 1.8 nm due to the variation of growing native silicon dioxide. If the SiO_2 thickness (d) is determined to be 0.9 nm and V is 2 V, the calculated current density ($J = I/A_{eff}$) is about 2.42 $*10^4$ A/cm^{2,} and transconductance g_m is around 10^5 S/cm^2. The calculated f_T (= $g_m/(2\pi C)$) is about tens of GHz. C denotes the net capacitance per area of the 0.9 nm SiO_2 capacitance and 4 nm hBN capacitance in series. This result means that by the device design (see **Figure 1a**), the maximum operation frequency of the GHET can reach GHz. However, the roughness of native silicon dioxide thickness makes the GHET cannot operate in such high frequency. For example, if the SiO_2 thickness is increased to 1.7 nm, g_m could dramatically decrease to 6.9 S/cm^2, and the cut-off frequency is only about a few MHz. That is the potential reason our specific devices can only operate in the MHz range owing to uncontrollable SiO_2 thickness variation. This result reveals that operation frequency limitation is due to uncontrollable thickness of native SiO_2, which is our device's emitter base tunneling barrier. The high-quality 2D materials insulator, like one-layer hBN with sub-one-nanometer thickness, would be one of the effective candidates for substitution for native SiO_2 to increase the operation frequency of the GHET.

References

1. A. C. Ferrari and D. M. Basko, *Nature Nanotechnology*, 2013, **8**, 235-246.
2. H. Kwon, S. Garg, J. H. Park, Y. Jeong, S. Yu, S. M. Kim, P. Kung and S. Im, *npj 2D Materials and Applications*, 2019, **3**, 9.
3. Y. Kubota, K. Watanabe, O. Tsuda and T. Taniguchi, *Science*, 2007, **317**, 932-934.
4. B. K. Sarker and S. I. Khondaker, *ACS nano*, 2012, **6**, 4993-4999.
5. J. M. Beebe, B. Kim, J. W. Gadzuk, C. D. Frisbie and J. G. Kushmerick, *Physical review letters*, 2006, **97**, 026801.
6. A. Laturia, M. Van de Put and W. Vandenberghe, *npj 2D Materials and Applications*, 2018, **2**.
7. J. Robertson, *The European Physical Journal-Applied Physics*, 2004, **28**, 265-291.
8. G.-H. Lee, Y.-J. Yu, C. Lee, C. Dean, K. L. Shepard, P. Kim and J. Hone, *Applied physics letters*, 2011, **99**, 243114.
9. B. Brar, G. Wilk and A. J. A. p. l. Seabaugh, 1996, **69**, 2728-2730.
10. Y. Liu, J. Sheng, H. Wu, Q. He, H. C. Cheng, M. I. Shakir, Y. Huang and X. Duan, *Advanced Materials*, 2016, **28**, 4120-4125.